Earth Planet. Sci. Lett. 633 (2024) 118651

Contents lists available at ScienceDirect

Earth and Planetary Science Letters

journal homepage: www.elsevier.com/locate/epsl

Crystallization of a hydrous magma ocean in the shallow lower mantle

Longjian Xie [a,b,c,*], Michael Walter [a,*], Tomoo Katsura [b], Fang Xu [d], Jianhua Wang [a], Yingwei Fei [a]

[a] Earth & Planets Laboratory, Carnegie Institution for Science, Washington, DC, 20015, USA
[b] Bayerisches Geoinstitut, University of Bayreuth, Bayreuth, 95440, Germany
[c] Department of Earth Sciences, University College London, London, WC1E6BS, UK
[d] Key Laboratory of Geoscience Big Data and Deep Resource of Zhejiang Province, School of Earth Sciences, Zhejiang University, Hangzhou, 310058, China

ARTICLE INFO

Dr. J. Badro

Keywords:
Magma ocean
Water
Silicate melt
Phase diagram
Lower mantle
High pressure

ABSTRACT

The solidification of a deep magma ocean occurred early in Earth's history. Although the initial amount of H_2O in Earth's magma ocean is predicted to be low (e.g., <3000 ppm), as an incompatible element it becomes highly enriched (e.g. >10 wt%) in the final few percent of crystallization. In order to understand how a hydrous magma ocean would crystallize at the top of the lower mantle, we determined liquidus phase relations in the MgO-FeO-CaO-Al_2O_3-SiO_2-H_2O system at 24 GPa. We find that the bridgmanite (brg) + stishovite (st) + melt and bridgmanite (brg) + ferropericlase (fp) + melt cotectic boundary curves trend to Mg-rich melt compositions with decreasing temperature and extend to very high H_2O contents (~80 mol% H_2O). The brg+st+melt curve is a subtraction curve at < ~18 mol% H_2O and a reaction curve at higher H_2O contents, whereas the brg+fp+melt is a subtraction curve throughout its length. The density of melts along the two cotectics leads to neutral buoyancy with respect to shallow lower mantle and transition zone minerals at H_2O contents up to ~25 mol%. A transient melt-rich layer can form at the top of the lower mantle during late-stage crystallization in a mushy magma ocean when melt percolation dominates. When crystallization exceeds ~98%, hydrous melts (>25 mol% H_2O) become buoyant and can percolate into and hydrate the mantle transition zone.

1. Introduction

1.1. Magma ocean crystallization and degassing

A deep or even whole-mantle magma ocean is believed to have been formed after the giant Moon-forming impact (Tonks and Melosh, 1993). Crystallization of a magma ocean can introduce primary mantle differentiation (Ballmer et al., 2017; Caro et al., 2005; Solomatov, 2007; Walter et al., 2004; Xie et al., 2021; 2020), and degassing of its volatile elements will have contributed to the formation Earth's post-impact atmosphere (Elkins-Tanton, 2008; Hamano et al., 2013; Lebrun et al., 2013; Miyazaki and Korenaga, 2022).

As a magma ocean crystallizes, the viscosity of magma abruptly changes from liquid-like to solid-like when the crystal fraction reaches ~60 vol.% (Pierru et al., 2022; Solomatov, 2007). In this study, we define the rheological front as the region with ~40% melt. The rheological front sweeps from the bottom-up or at least from the middle lower mantle as cooling proceeds, regardless of whether the magma ocean crystallizes from the bottom-up (Andrault et al., 2011; Boukaré et al., 2015; Monteux et al., 2020) or from the middle lower mantle outwards as predicted in some models (Labrosse et al., 2007; Nomura et al., 2011; Stixrude et al., 2009). Before the rheological front reaches the surface, the magma ocean is divided into a liquid-like layer and a solid-like layer by the rheological front (Ballmer et al., 2017; Hier--Majumder and Hirschmann, 2017; Lebrun et al., 2013; Maurice et al., 2017; Miyazaki and Korenaga, 2022). The former is mixed turbulently by rapid convection (Solomatov, 2007; Tonks and Melosh, 1990) and the latter is mixed by Rayleigh–Taylor instabilities (Elkins-Tanton, 2012; Maurice et al., 2017; Miyazaki and Korenaga, 2019). Rayleigh–Taylor instabilities continuously transport the newly formed solid-melt mush downwards because the downwelling velocity of the instability is faster than melt percolation (Solomatov, 2007).

Owing to the incompatibility of H_2O (Hirschmann et al., 2009; Kawamoto and Holloway, 1997) and the low initial H_2O content in the magma ocean (<3000 ppm) (Ohtani, 2021), low-degree trapped melts can hold most of the H_2O (~99%) in the deep mantle and the surface

* Corresponding authors.
E-mail addresses: ddtuteng@gmail.com (L. Xie), mwalter@carnegiescience.edu (M. Walter).

https://doi.org/10.1016/j.epsl.2024.118651
Received 16 November 2023; Received in revised form 18 January 2024; Accepted 1 March 2024
Available online 14 March 2024

magma ocean may not saturate and degass (Hier-Majumder and Hirschmann, 2017; Miyazaki and Korenaga, 2019). At this stage, although fractional solidification may occur in the liquid-like layer (Ballmer et al., 2017; Solomatov, 2007; Xie et al., 2021; 2020), most large-scale crystal fractionation should have been re-homogenized by the turbulent mixing process in the solid-like layer, which may be responsible for the near-chondritic trace and major element ratios (e.g. Ca/Al, *Sc*/Yb, Lu/Hf) in primitive upper mantle rocks (Corgne et al., 2005; Liebske et al., 2005; Walter et al., 2004). With a heat flux of $\sim 10^6$ (Solomatov, 2007), the magma ocean cools rapidly ($\sim 10^4$ years) at this stage (Monteux et al., 2016).

Once the rheological front reaches the surface, the viscosity of the whole magma ocean is solid-like, and solid-state convection governs cooling thereafter (Abe, 1997; Solomatov, 2007). At this stage, the mantle is comprised of solids plus trapped melt, and is entirely a mushy magma ocean. Modeling suggests that timescales of solid-state convection are slower than melt percolation (Lebrun et al., 2013; Miyazaki and Korenaga, 2022). The fate of low-degree melts in the mushy magma ocean depends on the density contrast between the melt and surrounding solids. Melts may percolate upward or downward depending on their buoyancy relative to the surrounding mantle. Buoyant melts may percolate upward all the way to the Earth's surface where they can erupt and degass to the atmosphere. Melts may also pond at depths where they become neutrally buoyant, retaining H_2O in the deep mantle.

The dihedral angle in the olivine-hydrous silicate melt system indicates a decrease with increasing pressure and temperature (Freitas and Manthilake, 2019; Yoshino et al., 2007) to nearly 0° below 440 km depth. If such a low dihedral angles apply, less than 1 vol.% melt is enough to completely wet grain boundaries. As a result, melt percolation can continue operating until complete drainage or crystallization of the trapped melt. Numerical simulation suggests that the mushy magma ocean cools slowly over ~200 million years (Monteux et al., 2020).

1.2. Compositional effect on the crystallization of magma ocean

The crystallizing behavior of a magma ocean is largely controlled by its composition. Of primary importance is the Mg/Si ratio, which determines whether ferropericlase or stishovite crystallizes together with bridgmanite (Liebske and Frost, 2012; Yao et al., 2021). The initial composition of a magma ocean involving near wholesale melting of the mantle will approximate the bulk silicate Earth (BSE) composition, which is the mean composition of the primary upper and lower mantles plus the crust. The composition of Earth's primitive upper mantle is well constrained from primitive lherzolite xenoliths and has a molar Mg/Si ratio of ~1.26 (McDonough and Sun, 1995). However, the composition of Earth's lower mantle is still debated, and seismic velocity and density data for the lower mantle are permissive of a range of Mg/Si ratios (Deng et al., 2023; Murakami et al., 2012). Another method to deduce the composition of the BSE is based on the bulk Earth (BE) composition and the core composition. The BE composition is also uncertain with the molar Mg/Si ratio potentially ranging from ~1.1 (carbonaceous chondrites) to ~0.7 (enstatite chondrites) based on the element abundances of primitive meteorites and the solar photosphere (e.g. Alexander, 2022). Due to the low solubility of Mg in molten Fe (Badro et al., 2018), we assume all the Mg was incorporated in the BSE. The Si content varies from 0 to ~4 wt% in the core (Hirose et al., 2021). Assuming 4 wt% Si in the core, the molar Mg/Si ratio of the BSE composition potentially ranges from ~1.2 to ~0.8.

In addition to the major elements, incompatible trace elements like H_2O can also have a large effect on magma ocean crystallization. The early BSE likely had a minor H_2O content, although the amount is highly uncertain, with recent estimates ranging from ~1000–3000 ppm H_2O or 2 to 8 ocean masses (Ohtani, 2021). As an incompatible element during deep mantle melting (e.g. Myhill et al., 2017), H_2O becomes highly concentrated in later-stage melts as a magma ocean crystallizes (e.g. 3 wt% at 90% crystallization for 3000 ppm H_2O and perfectly incompatible behavior). Recent simulations suggest that ~99% of the H_2O will remain in a highly crystalline, mushy magma ocean within interstitial melts (Miyazaki and Korenaga, 2022). Several pioneering studies have shown that such high levels of H_2O greatly affect liquidus phase relations by stabilizing a Si-rich phase in the lower mantle (Amulele et al., 2021; Nakajima et al., 2019; Shatskiy et al., 2007; Walter et al., 2015). Furthermore, H_2O decreases the solidus temperature of silicates (e.g. Myhill et al., 2017) and can extend crystallization to much lower temperatures. Indeed, the presence of H_2O has been postulated to cause melting in the lower mantle even along a modern geotherm (Schmandt et al., 2014). Therefore, quantifying the effect of H_2O on melting phase relations and constraining the positions of the three-phase cotectic liquidus boundaries, i.e., bridgmanite (brg) + stishovite (st) + melt and brg + ferropericlase (fp) + melt, is essential to model magma ocean crystallization in the lower mantle, especially at the mushy magma ocean stage.

Although melting phase relations of dry systems (e.g. Andrault et al., 2011; Fiquet et al., 2010; Ito et al., 2004; Zhang and Herzberg, 1994) and low water-bearing (<3 wt%) systems (Litasov and Ohtani, 2002) at lower-mantle conditions have been determined, the positions of the three-phase cotectics in the H_2O-rich peridotite system are not well constrained. This study aims at understanding magma ocean crystallization at the top of the lower mantle by determining liquidus phase relations in the (Mg, Fe, Ca)O-Al_2O_3-SiO_2-H_2O system at 24 GPa.

2. Methods

2.1. Starting material

The starting material was prepared based on the composition of a CI chondritic BSE with a molar Mg/Si ratio of 1.05 (McDonough and Sun, 1995). Reagent grade powders (SiO_2, Al_2O_3, FeO, MgO, $Mg(OH)_2$, $Al(OH)_3$, and $Ca(OH)_2$) were mixed in an appropriate ratio and hand-ground using an agate mortar and pestle. H_2O was added in the form of $Ca(OH)_2$, $Mg(OH)_2$, and $Al(OH)_3$ to match the CI-BSE bulk composition with target H_2O contents of 1.0, 5.0, 7.5, 10, and 15 wt%. To explore the effect of Fe, we also prepared an Fe-free starting material with the same model BSE composition with 10 wt% H_2O. To confirm the composition of the starting material, we synthesized the corresponding dry glass for each mixture by heating it to 1650 °C at one atmosphere and quenching in water. The glass was polished and analyzed by an electron microprobe analysis (EPMA) to accurately determine the composition (except H_2O) of the mixture, which is identical to that of the BSE model within analytical error (Supplementary Table 1).

2.2. High-pressure, high-temperature experiments

High-pressure, high-temperature conditions were generated in Kawai-type multi-anvil presses installed at the Bayerisches Geoinstitut, University of Bayreuth, Germany. WC cubes (Ha06) with 32 mm edge lengths and 3 mm truncation edge lengths were used as second-stage anvils. Supplementary Fig. 1 shows the cell assembly, which is a routine design used at Bayerisches Geoinstitut. A Cr-doped MgO (5 wt% Cr_2O_3) octahedron with a 7 mm edge length was used as a pressure medium, and $LaCrO_3$ was used for heaters. A $W_{75}Re_{25}$-$W_{97}Re_3$ thermocouple with 0.13 mm diameter was used to monitor the temperature. The temperature variation across the sample is less than 75 K (personal communication with Dr. Man at Bayerisches Geoinstitut, Germany). Pt was used as capsule material, and capsules were welded to ensure sealing. Sample capsules were weighed before and after welding and no significant differences were observed. Note that experiments with Pt as the outer capsule and Re as the inner capsule were made to check Fe loss (Table 1). However, Re reacted strongly with H_2O, affecting the bulk H_2O content of the sample and causing contamination. Thus only results of experiments using Pt as a capsule material are reported.

Table 1
Summary of experimental conditions and results.

Run No.	T, °C	Water in SM (wt%)	Fe-bearing or free	Capsule	st in cross sections	Fraction of st (wt%) *	First liquidus phase
H5415	1800	10	Bearing	Pt+Re	yes		st
	1800	15	Bearing	Pt+Re	yes		st
H5413	1900	10	Bearing	Pt	yes	4.2(2)	st
	1900	15	Bearing	Pt	yes	8.8(9)	st
S7709	1900	15	Bearing	Pt+Re	yes		st
	1900	10.35	Free	Pt	yes	3.6(1)	st
S7696	2000	10	Bearing	Pt	yes	3.8(3)	st
S7699	2100	1	Bearing	Pt	no		brg
	2100	5	Bearing	Pt	no	4(3)#	st
S7700	2100	5	Bearing	Pt	no	2(2) #	st
	2100	10	Bearing	Pt	yes	5.1(6)	st
S7705+	2100	7.5	Bearing	Pt	yes	1.8(5)	st
	2100	10.35	Free	Pt	yes	2.9(4)	st
H5410	2280	1	Bearing	Pt	no		brg
	2280	5	Bearing	Pt	no	1.1(4)	st
S7702	2370	1	Bearing	Pt	no		brg
	2370	5	Bearing	Pt	no	1.1(5)	st

SM: starting material.
st: stishovite.
* The amount of stishovite is calculated using a mass balance method.
+ In the Fe-free sample of S7705, a small amount of stishovite looked like grains were observed during the sample polishing process but were polished away later.
# The uncertainty is mainly contributed by the error of EPMA analysis and was estimated using a Monte Carlo method.

The cell assemblies were first compressed to 760 tonnes at room temperature, subsequently heated to the target temperature under the constant press load, and kept for 10 min. After heating, samples were quenched by cutting off the input power, decompressed, and recovered from the press. The recovered samples were polished for textural and chemical characterization by SEM and EPMA.

2.3. Electron microprobe analysis of recovered samples and the glass of starting material

The compositions of recovered samples and the glass of the starting material were measured by electron microprobe analysis (EPMA) at Bayerisches Geoinstitut, Unversity of Bayreuth, Germany. Re, Pt, Fe, diopside, spinel, and enstatite were used as standards. An accelerating voltage of 15 kV was used. A beam size of 1 μm was adopted for the solid and metallic capsule analysis. For the glass and large melt portions, a combination of a defocused beam (10 μm) and rectangular scanning (commonly 60 × 60 μm) with a step of 10 μm was adopted to measure an average composition. In Run S7699 and S7700, the recovered samples have a small melt portion, and a defocused spot beam was adopted for the melt analysis in these samples.

2.4. Nano-SIMS analysis of water content analysis in the coexisting solid phases

The water contents in the coexisting solid phases were measured at the Earth & Planets Laboratory, Carnegie Institution of Washington, with the CAMECA nanoSIMS 50 L using methods developed for the microanalysis of trace amounts of H_2O, CO_2, F, S, and Cl in glasses and nominally anhydrous minerals (Hauri et al., 2002; Newcombe et al., 2023; Peterson et al., 2023; Shimizu et al., 2021). The vacuum in the analysis chamber was maintained at a pressure of ~5 × 10^{-10} torr to minimize the background and improve detection limits. The ~2 nA Cs^+ primary beam was accelerated to 16 keV and focused to a spot size of ~2 μm. Prior to each analysis, the standard and sample surface was pre-sputtered by rastering the primary beam over a 15 × 15 μm^2 area for 5 min to remove the Au coat and sputter away the surface contamination. For the analysis, the raster was reduced to 10 × 10 μm^2 and only the area of the center of 5 × 5 μm^2 was collected to determine the concentration of these volatiles. The secondary ions $^{12}C^-$, $^{16}OH^-$, $^{17}F^-$, $^{30}Si^-$, $^{32}S^-$, and $^{35}Cl^-$ were simultaneously collected with entrance slit 4 and aperture slit 4. The mass resolving power was ~9000, sufficient to separate ^{17}O from ^{16}OH. The electron gun was used to compensate for the charge generated on the sample surface due to the implantation of Cs^+ ions and extraction of negatively charged secondary ions and electrons. Each spot analysis took about 15 min and 3 repeated analyses were performed on each sample. A series of basaltic glass standards were used for data calibration. The background of H_2O is less than 4 ppm (2σ) and the error of the analyses is less than 10% (2σ).

3. Results

3.1. Coexisting phases

Table 1 summarizes the experimental conditions and results. We identified partial melts and coexisting solid phases through back-scattered electron imaging of sectioned and polished recovered samples (Fig. 1). The quenched melt phase was comprised of irregular, feathery crystals plus voids. We interpret the voids as having been occupied by an exsolved fluid phase upon quenching since fluid and melt are immiscible below about 4 GPa and 1000 °C in the peridotite-H_2O system (Mibe et al., 2007; Wang et al., 2020). We observed changes in coexisting liquidus phases from brg to brg + st in starting compositions containing 7.5 wt% H_2O. We further observed that stishovite is always present at the melt-solid boundary and that its modal abundance increases with increasing H_2O content in the starting mixture. The presence of stishovite at the melt-solid boundary is consistent with expectations for thermal diffusion in a saturation gradient (Lesher and Walker, 1988).

In order to constrain phase proportions in the experiments quantitatively, mass balance calculations were performed on an anhydrous basis using the compositions of the starting material and the coexisting phases in each run (see details in Supplementary Text 1). The calculations confirm the presence of stishovite in samples containing ≥7.5 wt% H_2O and show a positive correlation between stishovite fraction and the H_2O content of bulk samples (Supplementary Fig. 2a). The mass balance results further indicate that stishovite should just appear in experiments containing 5 wt% H_2O, although it was not observed in the experimental polished cross-section (Fig. 1). This minor discrepancy between the mass balance calculations and the cross-section observations could result from the challenge of detecting a small amount of stishovite when imaging a single cross-section in samples.

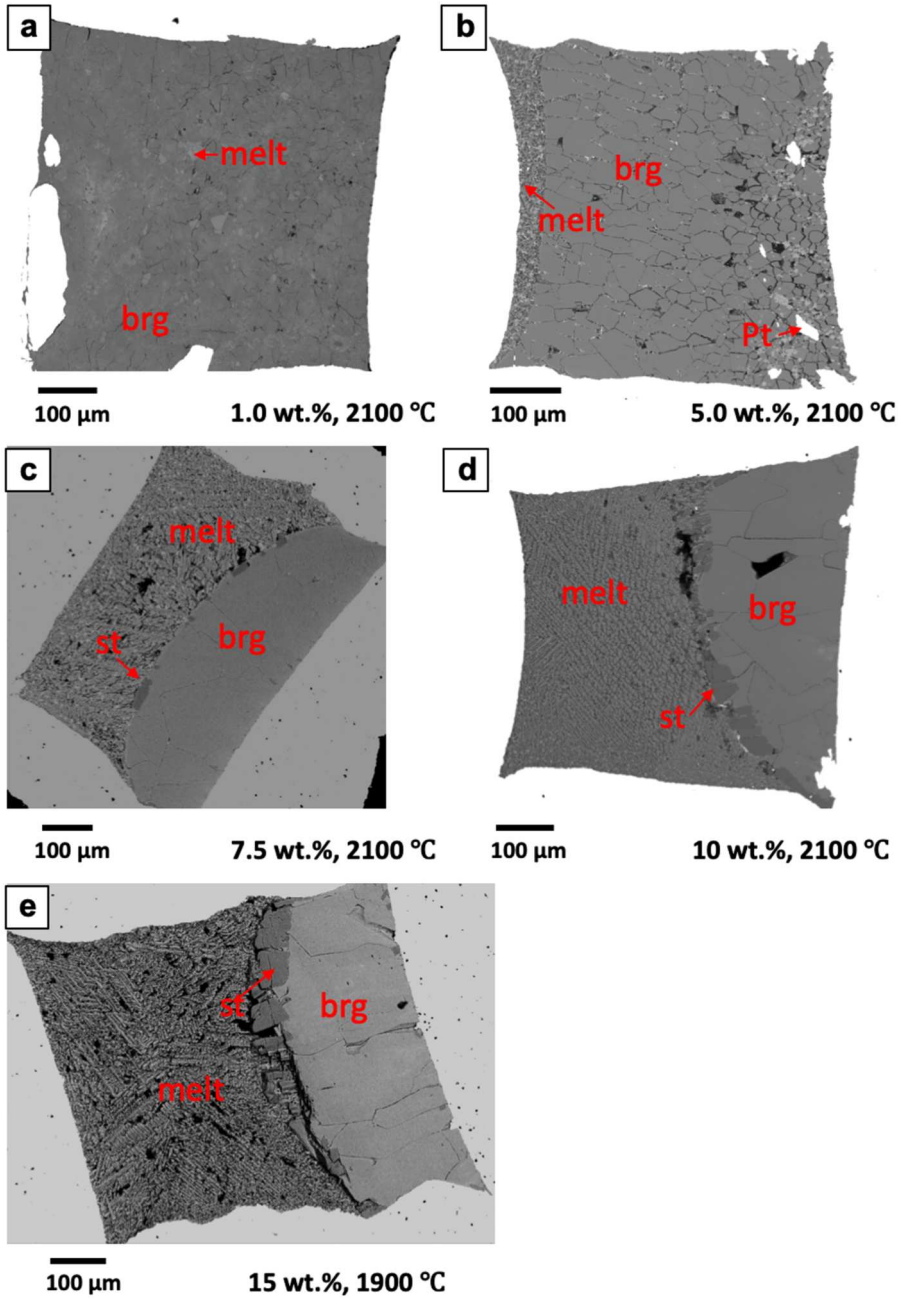

Fig. 1. Representative backscattered images of recovered samples. fp: ferropericlase, brg: bridgmanite, st: stishovite, Pt: platinum.

3.2. Chemical compositions of the coexisting phases

The chemical compositions of the coexisting phases are presented in Supplementary Table 2. The melts are enriched in Ca and Fe, while the coexisting bridgmanite is almost Ca-free but Fe-bearing. The apparent bridgmanite-melt Fe partition coefficient, defined as $K_D = (Fe/Mg)_{bridgmanite}/(Fe/Mg)_{melt}$, is between 0.4 and 0.5 and slightly increases with water content (Supplementary Fig. 7a). Both bridgmanite and stishovite are Al-bearing, with an Al_2O_3 content of ~ 4 wt% and ~ 2 wt %, respectively. The bulk water content has little effect on their Al_2O_3 content.

To check for Fe loss to Pt capsules, we also examined the Fe content of the polished capsules using EPMA. For samples with high water contents (≥5 wt%) and heated to relatively lower temperatures (<2280 °C), the Fe content in Pt capsule is below the detection limit (~0.1 wt%), which is consistent with previous results in the presence of a large amount of H_2O (Amulele et al., 2021). Only small Fe loss (<1%) was detected in the samples containing 1 or 5 wt% H_2O and heated to temperatures higher than 2280 °C. The short run duration (~10 min) at the target temperature may also limit Fe loss into the Pt capsule.

3.3. Water content in the melt

The H_2O content in the melt cannot be directly determined from the sample as the melts produced in our experiments did not quench to glass. In previous studies, the H_2O content of the melt was estimated either from the deficit of the total of the EPMA analysis (Nakajima et al., 2019) or from the void volume and equation of state for H_2O (Amulele et al., 2021). However, the void method requires assumptions about the density of the quenched melt.

In this study, we used 3 methods to constrain the H_2O content of melts. The first method utilizes the EPMA deficit from 100%. The second

method utilizes the water content of the starting material and the resulting melt fraction. We assumed no H_2O was lost during the experiments and all the H_2O was in the melt as the H_2O content in the coexisting solids is 2 orders of magnitude smaller. The H_2O content in the melt was estimated from the H_2O content in the starting material divided by the melt fraction calculated in the mass balance. The H_2O content estimated by this method represents an upper limit but is consistent with that estimated by the total deficit of EPMA analysis (Supplementary Fig. 3). In the third method the coexisting solid phases and the measured ratio of (Mg, Fe, Ca)/(Si, Al) of the melts were used to bracket the H_2O content of the melt (Supplementary Fig. 4). Although the range of estimated H_2O contents in each run is large in this method, the brg+st+melt boundary is tightly constrained as it must continuously and smoothly pass through all the compositions of the melts coexisting with brg+st (Supplementary Fig. 6a).

All three methods give consistent estimations (Supplementary Fig. 3 and Supplementary Fig. 6a). For starting materials containing 5, 7.5, 10, 15 wt% of H_2O, the H_2O contents of the melts ranged from 6 to 21, around 13, from 17 to 30, and from 27 to 42 wt%, respectively.

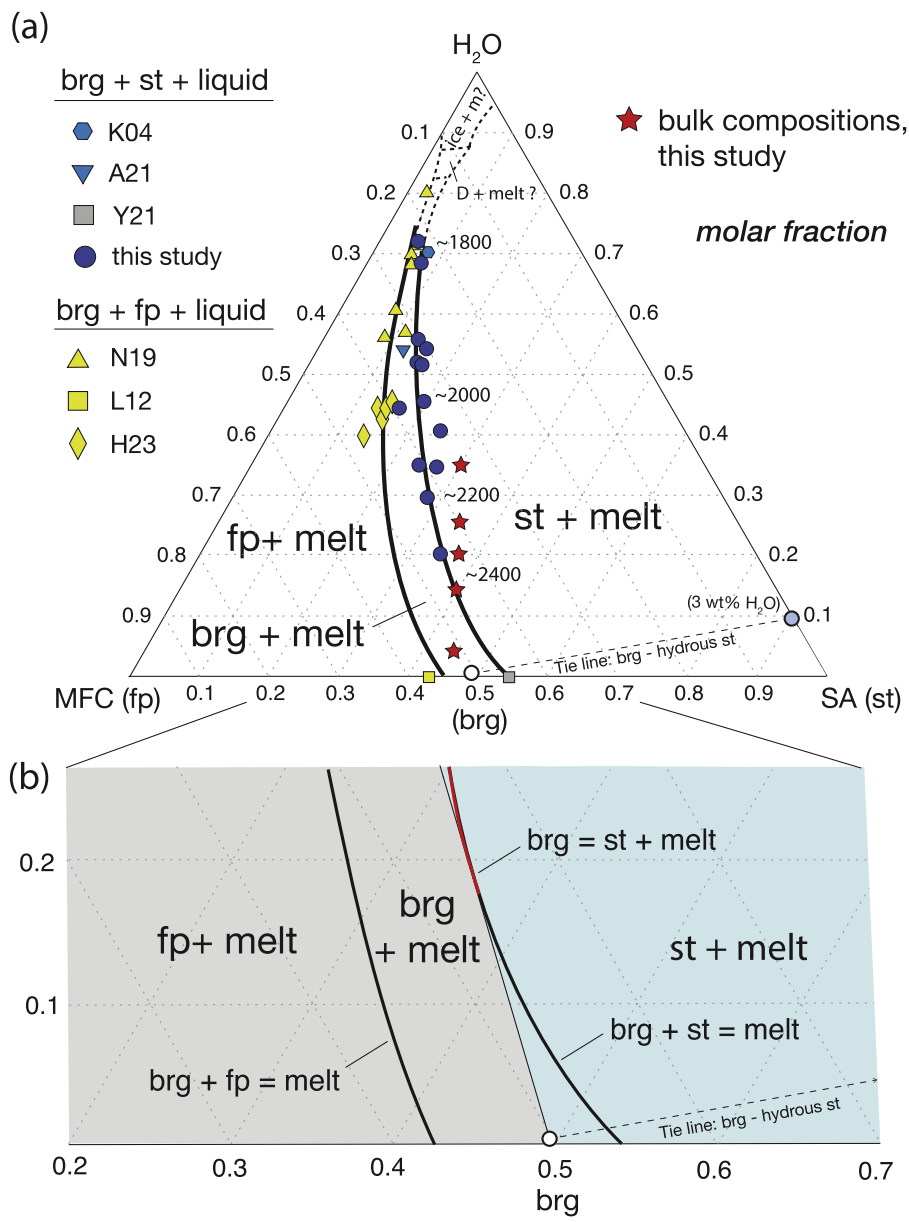

Fig. 2. Melting phase relationships in the (Mg, Fe, Ca)O-SiO_2-Al_2O_3-H_2O system projected onto the pseudo-ternary (Mg, Fe, Ca)O (MFC)-SiO_2+Al_2O_3 (SA)-H_2O in molar fraction. **(a)** The brg + st + melt and brg + fp + melt boundaries as constrained by this study and previous results. The H_2O contents of melt were estimated by mass balance. Phase relations in the H_2O-rich end of the diagram are schematic only. st: stishovite, brg: bridgmanite, fp: ferropericlase, D: phase D. Y21: data from Yao et al., 2021 at ~24 GPa and 2480 °C (Yao et al., 2021); K04: data from Kawamoto 2004 at ~24 GPa and 1400 °C (Kawamoto, 2004); A21: data from Amulete et al., 2021 at ~25 GPa and ~1600 °C (Amulele et al., 2021); H23: data from Huang et al., 2023 at 25 GPa and 1700 °C (Huang et al., 2023); N19: data from Nakajima et al., 2019 at pressures 23.5 and 26 GPa and temperatures from 1400 to 1590 °C (Nakajima et al., 2019); L12: data from Liebske et al. 2012 at 24 GPa and ~2440 °C (Liebske and Frost, 2012). **(b)** Phase relations along the brg + st + melt and brg + fp + melt boundary curves. The thin line shows a tangent along the brg + st + melt boundary corresponding to a change from a subtraction curve at H_2O contents < ~18 mol% (brg + st = melt) to a reaction curve at higher H_2O contents (brg = st + melt). The thin line also separates bulk compositions that will reach the brg + st + melt boundary (blue region) from those that will reach the brg + fp + melt boundary (gray region). The brg + fp + melt boundary is a subtraction curve all along its length (brg + fp = melt).

3.4. Water content in the coexisting solid phases

The H_2O content in stishovite and bridgmanite obtained in samples with various bulk water contents are provided in Supplementary Table 3. The H_2O content in bridgmanite varies from 630 to 1058 ppm among 11 points across two samples, with an average value of 870 (140) ppm. There is no apparent correlation with bulk water content or temperature. Our result is consistent with recent studies where H_2O in bridgmanite equilibrated with hydrous silicate melt was measured using Fourier-transform infrared spectroscopy (Fu et al., 2019) and SIMS (Yang et al., 2023). The H_2O content in stishovite varies from 2800 to 3200 ppm, with an average value of 3050 (150) ppm, which is consistent with the FTIR-measured values in Al-bearing stishovite (Litasov et al., 2007). Hydrogen incorporation has been suggested to be through substitution of octahedral (Si^{4+}) by (H^{+} +Al^{3+}) (Litasov et al., 2007). In contrast, recent studies indicate that H_2O can reach weight percent levels in stishovite at high pressures, apparently inconsistent with our measured values (Lin et al., 2022; 2020; Nisr et al., 2020). However, H_2O has been shown to be incorporated interstitially in stishovite possibly as one-dimensional water channels (Kueter et al., 2023; Li et al., 2023; Lin et al., 2022), and Lin et al. (2020, 2022) show that most of the H_2O can be lost on decompression to ambient conditions. Therefore, the measured values of recovered stishovite represent the remaining water content and, thus, the lower limit of the H_2O content at high pressure.

Mineral/melt partition coefficients ($D^{min/melt}$) for H_2O are summarized in Supplementary Table 4. $D^{brg/melt}$ ranges from 0.003 to 0.007, attesting to its incompatibility. $D^{st/melt}$ for H_2O is uncertain due to the possible loss of H_2O on decompression. Based on the measured values they range from 0.01 to 0.02. However, using a value of 3 wt% H_2O, as indicated by the calibration of Lin et al. (2022), $D^{st/melt}$ would be of the order 0.1 – 0.2.

4. Discussions

4.1. Liquidus phase boundaries

The brg + st + melt and brg + fp + melt boundary curves are constrained from observed melt compositions determined in this and previous experimental studies. A polynomial was fitted to the H_2O content as a function of (Mg, Fe, Ca)O/(SiO_2+Al_2O_3) ratio for the melt compositions, combined with additional eutectic data for the brg + st + melt (Yao et al., 2021) and brg + fp + melt (Liebske and Frost, 2012) in the anhydrous MgO-SiO_2 system (Supplementary Fig. 5). The fitted functions representing the phase boundaries are shown on a pseudo-ternary projection (mol%) in Fig. 2. Boundary curves constrained from H_2O contents estimated from all three methods are similar to each other, especially for H_2O contents below 40 mol% (Supplementary Fig. 6b). The bulk compositions of experiments with and without stishovite bracket the brg + st + melt boundary; bulk composition with 5 wt% H_2O coincidently falls on the fitted brg + st + melt boundary, consistent with the mass balance calculation indicating minor stishovite. Both boundary curves trend to more MgO-rich melt compositions and have a shape that is concave to the SiO_2-rich side of the diagram (Fig. 2). These observations are consistent with liquidus boundary curves in the MgO-SiO_2-H_2O system at 13 GPa that show a similar trend to MgO-rich compositions with increasing H_2O content (Myhill et al., 2017).

Fig. 2b shows the two boundary curves at H_2O contents less than ~25 mol% H_2O. Treating the phase relations as strictly ternary for simplicity, we predict that the brg + fp + melt boundary curve is a subtraction curve over its entire extent (brg + fp = melt), where both bridgmanite and ferropericlase crystallize from the melt upon cooling (i.e. all lines tangent to the boundary curve intersect at a point between bridgmanite and ferropericlase). In contrast, the brg + st + melt boundary curve is a subtraction curve (brg + st = melt) up to ~18 mol% H_2O but becomes a reaction curve at higher H_2O contents along which stishovite reacts with melt to form bridgmanite (brg = st + melt); at H_2O contents greater than ~18 mol% lines tangent to the boundary curve do not intersect between bridgmanite and stishovite but at a point between bridgmanite and ferropericlase. During equilibrium crystallization, all bulk compositions in the shaded blue region in Fig. 2b will crystallize along the brg + st + melt boundary curve, whereas those in the gray-shaded region will crystallize along the brg + fp + melt boundary curve.

4.2. Melt composition evolution during magma ocean solidification

Equilibrium crystallization paths for five different potential bulk silicate magma ocean compositions are deduced from the phase relations in Fig. 3. Bulk compositions spanning a range of plausible Mg/Si molar ratios are considered and include: (1) a 'pyrolytic' composition (Mg/Si = 1.09) (Wang et al., 2018); (2) a CI chondrite composition (Mg/Si=1.05) (McDonough and Sun, 1995); (3) an EH chondrite composition (Mg/Si=0.73) (Wasson and Kallemeyn, 1988); (4) the enstatite chondrite model of Javoy et al. (2010) (Mg/Si=0.79); (5) a constructed composition of 71% EH chondrite, 24% ordinary chondrite and 5% CM chondrite mimicking the model of Dauphas (2017) (Mg/Si=0.80). In constructing model BSE compositions, a core comprising 32 wt% of Earth's mass was subtracted from model bulk Earth compositions using the model iron-alloy composition with 0–4 wt % Si of Hirose et al. (2021). The model BSE presented in McDonough and Sun (1995) is used for CI chondrite, which arbitrarily assumes 8 wt % FeO in the BSE. Hereafter, we refer to these BSE compositions as Py-BSE (1.16<MCF/SA<1.27), CI-BSE (1.02<MCF/SA<1.28), EH-BSE (0.80<MCF/SA<0.86), Javoy-BSE (0.91<MCF/SA<0.98), and Dauphas-BSE (0.84<MCF/SA<0.91), respectively. The H_2O content of Earth's magma ocean is not known with certainty. Bulk silicate Earth models (e.g. Halliday, 2013; Hirschmann, 2018; Marty, 2012) suggest about 500–1000 ppm although much more is possible (Peslier et al., 2017). Fig. 3a illustrates how these different BSE compositions would

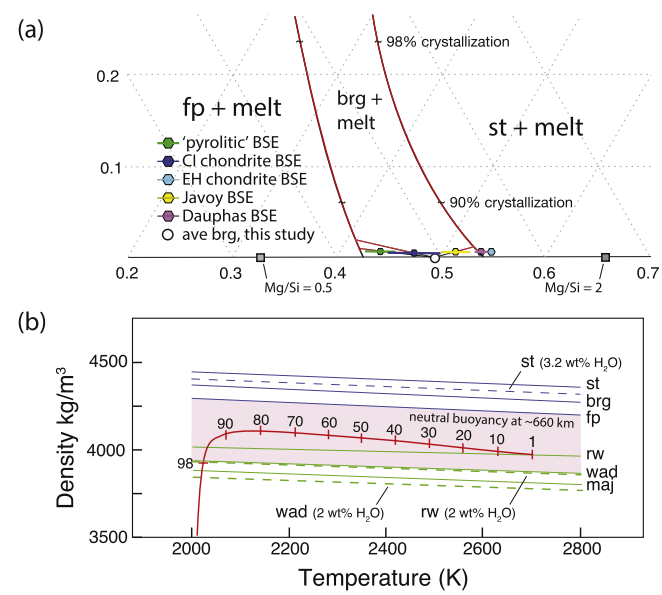

Fig. 3. **(a)** Equilibrium crystallization of model BSE compositions according to the observed phase relations in Fig. 2. Estimates are given for the degree of crystallization along the brg + st + melt boundary curve. The red curves show melt evolution for equilibrium crystallization. **(b)** Density evolution of melt at 24 GPa during the solidification of magma ocean based on the model of Drewitt et al. (2022). The red curve shows the density evolution with the degree of equilibrium crystallization demarked along the curve. Density evolution is almost identical along the brg + fp + melt boundary curve. Solid and dashed lines indicate the densities of dry (Stixrude and Lithgow-Bertelloni, 2011 and references therein) and water-bearing (Chang et al., 2015; Nisr et al., 2017) mantle minerals, respectively. brg: bridgmanite; fp: ferropericlase; rw: ringwoodite; st: stishovite; wad: wadsleyite, maj: majorite.

crystallize. As the paths are not sensitive to our choice of H_2O content, a value of ~2000 ppm (~0.6 mol%) is used for illustrative purposes.

For the bulk compositions whose liquidus phase is bridgmanite, equilibrium crystallization forces melt compositions to either higher or lower MCF/SA. For pyrolite and CI-BSE compositions liquidus bridgmanite crystallization forces melts to higher MCF/SA, reaching the brg+fp+melt boundary after ~30 mol% and ~70 mol% crystallization, respectively. Conversely, for the Javoy-BSE composition, the MCF/SA ratios of melts decrease as bridgmanite crystallizes until they intersect the brg+st+melt boundary curve at ~50 mol% bridgmanite crystallization. For the EH-BSE and Dauphas-BSE compositions, stishovite is the liquidus phase and equilibrium crystallization forces melt compositions to higher MCF/SA, reaching the brg+st+melt boundary curve after ~5 mol% stishovite crystallization for EH-BSE, ~1% crystallization for Dauphas-BSE.

Thus, cooling and crystallization of the magma ocean will result in melts evolving along either of the two cotectic boundary curves to become increasingly H_2O-rich as crystallization proceeds. For our model H_2O contents, melts on both boundary curves will contain ~ 6 mol% H_2O by 90% crystallization and ~25 mol% H_2O by ~98% crystallization (Fig. 3a). The last stages of equilibrium crystallization (< 1% melt) can lead to very high H_2O contents (e.g. ~80 mol% H_2O) possibly at a pseudo-invariant point involving bridgmanite, ferropericlase or stishovite, and phase D (Fig. 2).

We note that fractional crystallization will produce the same path of melt evolution as equilibrium crystallization for the pyrolite and CI-BSE compositions. For compositions crystallizing along the brg+st+melt boundary curve, fractional crystallization would cause the melt composition to move off the boundary curve at ~18 mol% H_2O where the boundary curve becomes a reaction curve (brg = st + melt), into the brg+melt field where only bridgmanite crystallizes, and eventually evolving along the brg+fp+melt boundary curve. However, regardless of the bulk composition, initial magma ocean water content, and crystallization style, a crystallizing magma ocean will lead to very high melt H_2O contents during the later stages of magma ocean crystallization.

4.3. Density evolution of residual melt at the top of the lower mantle

We use recent calculations and modeling of the density of hydrous melts in the system MgO-FeO-SiO_2-H_2O (Drewitt et al., 2022) to estimate the densities of hydrous melts at 24 GPa. The densities of melts along the brg + st + melt boundary are shown in Fig. 3b; the results are almost identical for the brg + fp + melt boundary. Also shown are the densities of brg, fp and st (both anhydrous and with 3.2 wt% H_2O), all of which are significantly more dense throughout the crystallization path. In the uppermost lower mantle hydrous melts are less dense than coexisting solids (brg, fp, st), and we speculate that this will remain true throughout the lower mantle, such that hydrous melts should be buoyant.

At ~660 km bridgmanite + ferropericlase react to form ringwoodite in bulk compositions with Mg/Si > ~1, whereas in compositions with Mg/Si < ~1 bridgmanite transforms to majorite garnet. Hydrous melts along the boundary curves are expected to be denser than phases crystallized in the upper mantle (e.g. hydrous ringwoodite, hydrous wadsleyite, majorite) until about 98% crystallization, where melts contain ~25 mol% H_2O (~10 wt% H_2O); values are only slightly variable among the bulk compositions in Fig. 3.

It is notable that low-degree melting in the modern mantle induced by fluxing of water from subducted lithosphere near the top of the lower mantle (e.g. Shirey et al., 2021) will produce a melt that is highly enriched in H_2O (e.g. > 50 mol%), and based on the modeled density will be buoyant relative to lower mantle and transition zone assemblages. Such melt should migrate out of the lower mantle and into the transition zone rather than remaining ponded in the lower mantle (Drewitt et al., 2022). In this case, seismic evidence interpreted as low-degree hydrous melting at the top of the lower mantle (Schmandt et al., 2014) may be imaging transient rather than neutrally buoyant melts.

Because of the vigorous mixing in a liquid-dominated magma ocean, ponding of melt should not occur at the top of the lower mantle even though melt is neutrally buoyant there. However, in a mushy magma ocean where crystalline rheology dominates, solid-state convection is slower than melt percolation and ponding of neutrally buoyant melt can occur (Lebrun et al., 2013; Miyazaki and Korenaga, 2022). Furthermore, the viscosity of dry silicate melts at lower-mantle conditions is measured to be low, of the order 10 mPa.s (Xie et al., 2021; 2020), and theoretical simulation suggests that the viscosity of silicate melt decreases with increasing H_2O content (Drewitt et al., 2022; Karki et al., 2021). Consequently, hydrous melt could efficiently segregate from the convecting mantle with a slight density contrast (e.g. of the order 10 kg/m^3). Therefore, between about ~60 to 98% crystallization when magma is a mush, the top of the lower mantle is a potential location to pond hydrous melts in interstitial pores, forming a transient melt-rich layer.

We conjecture that because of the considerable lowering of the lower mantle peridotite solidus by the presence of H_2O (e.g. hydrous melting can occur in the lower mantle even along a modern geotherm), a neutrally buoyant melt layer beneath 660 km is likely to occur as the last vestiges of melt crystallize in a magma ocean. The size of the transient melt-rich ponded layer is governed by the H_2O budget during crystallization, which will depend on the initial magma ocean H_2O content among other factors such as the solubility of H into the core, the efficiency of surface degassing, and potentially the sequestration into a basal melt layer (Labrosse et al., 2007). The layer may be from meters to hundreds of km thick depending on these contingencies. However, in any case the H_2O concentration in the layer will reach very high levels (e.g. >25 mol%) during the latter stages of crystallization regardless of the thickness of the layer. Once the magma ocean reaches ~98% crystallization we predict its residual melt will become buoyant relative to transition zone minerals constituting the upper boundary of the ponded layer (Fig. 3), and percolate into and hydrate the transition zone.

The crystallization scenario suggested by our results indicates that the transition zone would be among the last mantle layers to become hydrated during magma ocean solidification. Dong et al. (2021) estimate the storage capacity of the transition zone at Hadean temperatures post magma ocean solidification to be ~3×10^{20} kg H_2O (Dong et al., 2021). Assuming that ~3×10^{20} kg H_2O was retained by the ponded melt at ~660 km depth when 98% of the magma ocean was crystallized, the thickness of the melt-rich layer depends on the layer's melt fraction. For a mush layer 98% crystalline and with ~10 wt% H_2O, the mush layer would need to be ~100 km thick to fully hydrate the transition zone from an initially anhydrous state, i.e. this is a maximum thickness. We suggest that a late-stage ponded hydrous mushy melt layer at the top of the lower mantle likely assured a transition zone at or near its H_2O storage capacity after complete magma ocean solidification, regardless of its initial H_2O content.

5. Conclusions

We constrained the location of the brg + st + melt and brg + fp + melt boundary curves in the (Mg, Fe, Ca)O-Al_2O_3-SiO_2-H_2O system at 24 GPa. These phase boundaries have been applied to depict the path of melt evolution during crystallization of Earth's magma ocean. A crystallizing magma ocean will lead to very high melt H_2O contents during the later stages of magma ocean crystallization. Density modeling suggests that hydrous melts along the boundary curves are expected to be denser than phases crystallized in the upper mantle but less dense than phases crystallized in the lower mantle until about 98% crystallization. The neutral buoyancy of melt could lead to a ponded melt layer at ~660 km depth in the mushy magma ocean when solid-state convection is slower than melt percolation. When crystallization exceeds ~98%, hydrous interstitial melts (>25 mol% H_2O) become buoyant relative to

lower mantle and transition zone phases, and can therefore migrate into and hydrate minerals in the mantle transition zone.

Data availability

The authors declare that the majority of the data supporting the findings of this study are available in the paper or in supplementary materials. The unpublished data are available from the corresponding author upon request.

CRediT authorship contribution statement

Longjian Xie: Writing – review & editing, Writing – original draft, Visualization, Validation, Project administration, Methodology, Investigation, Formal analysis, Data curation, Conceptualization. **Michael Walter:** Writing – review & editing, Writing – original draft, Visualization, Validation, Supervision, Resources, Conceptualization. **Tomoo Katsura:** Writing – review & editing, Visualization, Supervision, Resources, Conceptualization. **Fang Xu:** Writing – review & editing, Validation. **Jianhua Wang:** Writing – review & editing, Investigation. **Yingwei Fei:** Writing – review & editing, Supervision, Resources, Conceptualization.

Declaration of competing interest

The authors declare that they have no known conflicts of interest to disclose.

Acknowledgments

We thank R. Njul and D. Krauße at Bayerisches Geointitut (Germany) for their help in polishing the sample and EPMA measurement, respectively. We thank Dr. Conel Alexander at Earth & Planets Laboratory (USA) for the discussion about chondritic materials and preparation of the Nano-SIMS sample, Dr. Man at Bayerisches Geoinstitut (Germany) for the discussion about the thermal gradient within 7/3 BGI cell assembly. We also thank Editor Badro, Dr. Corgne, and Dr. Boukaré for their constructive comments. This work was supported by a Carnegie Fellowship to L. Xie. Y. Fei acknowledges support from the National Science Foundation-Earth Sciences (EAR-2022492). T. Katsura acknowledges support from the European Research Council (ERC) under the European Union's Horizon 2020 research and innovation programme (Proposal No. 787527) and from Deutsche Forschungsgemeinschaft (DFG, German Research Foundation) - Project numbers: KA3434/24-1, KA3434/20-1, and KA3434/19-1.

Supplementary materials

Supplementary material associated with this article can be found, in the online version, at doi:10.1016/j.epsl.2024.118651.

References

Abe, Y., 1997. Thermal and chemical evolution of the terrestrial magma ocean. Phys. Earth Planet. Interior. 100, 27–39. https://doi.org/10.1016/S0031-9201(96)03229-3.

Alexander, C.M.O., 2022. An exploration of whether Earth can be built from chondritic components, not bulk chondrites. Geochim. Cosmochim. Acta 318, 428–451. https://doi.org/10.1016/j.gca.2021.12.012.

Amulele, G., Karato, S., ichiro, Girard, J., 2021. Melting of bridgmanite under hydrous shallow lower mantle conditions. J. Geophys. Res. Solid. Earth. 126 https://doi.org/10.1029/2021JB022222.

Andrault, D., Bolfan-Casanova, N., Nigro, G.Lo, Bouhifd, M.A., Garbarino, G., Mezouar, M., 2011. Solidus and liquidus profiles of chondritic mantle: implication for melting of the Earth across its history. Earth. Planet. Sci. Lett. 304, 251–259. https://doi.org/10.1016/j.epsl.2011.02.006.

Badro, J., Aubert, J., Hirose, K., Nomura, R., Blanchard, I., Borensztajn, S., Siebert, J., 2018. Magnesium partitioning between earth's mantle and core and its potential to drive an early exsolution geodynamo. Geophys. Res. Lett. 45 https://doi.org/10.1029/2018GL080405.

Ballmer, M.D., Lourenço, D.L., Hirose, K., Caracas, R., Nomura, R., 2017. Reconciling magma-ocean crystallization models with the present-day structure of the Earth's mantle. Geochem. Geophys. Geosyst. 18, 2785–2806. https://doi.org/10.1002/2017GC006917.

Boukaré, C.E., Ricard, Y., Fiquet, G., 2015. Thermodynamics of the MgO-FeO-SiO_2 system up to 140 GPa: application to the crystallization of Earth's magma ocean. J. Geophys. Res. Solid. Earth. 120, 6085–6101. https://doi.org/10.1002/2015JB011929.

Caro, G., Bourdon, B., Wood, B.J., Corgne, A., 2005. Trace-element fractionation in Hadean mantle generated by melt segregation from a magma ocean. NatureNature 436, 246–249. https://doi.org/10.1038/nature03827.

Chang, Y., Jacobsen, S.D., Bina, C.R., Thomas, S., Smyth, J.R., Frost, D.J., Boffa Ballaran, T., McCammon, C.A., Hauri, E.H., Inoue, T., Yurimoto, H., Meng, Y., Dera, P., 2015. Comparative compressibility of hydrous wadsleyite and ringwoodite: effect of H_2O and implications for detecting water in the transition zone. J. Geophys. Res. Solid. Earth. 120, 8259–8280. https://doi.org/10.1002/2015JB012123.

Corgne, A., Liebske, C., Wood, B.J., Rubie, D.C., Frost, D.J., 2005. Silicate perovskite-melt partitioning of trace elements and geochemical signature of a deep perovskitic reservoir. Geochim. Cosmochim. Acta 69, 485–496. https://doi.org/10.1016/j.gca.2004.06.041.

Dauphas, N., 2017. The isotopic nature of the Earth's accreting material through time. Nature 541, 521–524.

Deng, X., Xu, Y., Hao, S., Ruan, Y., Zhao, Y., Wang, W., Ni, S., Wu, Z., 2023. Compositional and thermal state of the lower mantle from joint 3D inversion with seismic tomography and mineral elasticity. Proc. Natl. Acad. Sci. 120 https://doi.org/10.1073/pnas.2220178120.

Dong, J., Fischer, R.A., Stixrude, L.P., Lithgow-Bertelloni, C.R., 2021. Constraining the volume of earth's early oceans with a temperature-dependent mantle water storage capacity model. AGU Adv. 2 https://doi.org/10.1029/2020AV000323.

Drewitt, J.W.E., Walter, M.J., Brodholt, J.P., Muir, J.M.R., Lord, O.T., 2022. Hydrous silicate melts and the deep mantle H_2O cycle. Earth. Planet. Sci. Lett. 581 https://doi.org/10.1016/j.epsl.2022.117408.

Elkins-Tanton, L.T., 2012. Magma oceans in the inner solar system. Annu Rev. Earth. Planet. Sci. 40, 113–139. https://doi.org/10.1146/annurev-earth-042711-105503.

Elkins-Tanton, L.T., 2008. Linked magma ocean solidification and atmospheric growth for Earth and Mars. Earth. Planet. Sci. Lett. 271, 181–191. https://doi.org/10.1016/j.epsl.2008.03.062.

Fiquet, G., Auzende, A.L., Siebert, J., Corgne, A., Bureau, H., Ozawa, H., Garbarino, G., 2010. Melting of peridotite to 140GPa. Science (1979) 329, 1516–1518.

Freitas, D., Manthilake, G., 2019. Electrical conductivity of hydrous silicate melts: implications for the bottom-up hydration of Earth's upper mantle. Earth. Planet. Sci. Lett. 523, 115712 https://doi.org/10.1016/j.epsl.2019.115712.

Fu, S., Yang, J., Karato, S., ichiro, Vasiliev, A., Presniakov, M.Y., Gavrilliuk, A.G., Ivanova, A.G., Hauri, E.H., Okuchi, T., Purevjav, N., Lin, J.F., 2019. Water concentration in single-crystal (al,fe)-bearing bridgmanite grown from the hydrous melt: implications for dehydration melting at the topmost lower mantle. Geophys. Res. Lett. 46, 10346–10357. https://doi.org/10.1029/2019GL084630.

Halliday, A.N., 2013. The origins of volatiles in the terrestrial planets. Geochim. Cosmochim. Acta 105, 146–171. https://doi.org/10.1016/j.gca.2012.11.015.

Hamano, K., Abe, Y., Genda, H., 2013. Emergence of two types of terrestrial planet on solidification of magma ocean. Nature 497, 607–610. https://doi.org/10.1038/nature12163.

Hauri, E., Wang, J., Dixon, J.E., King, P.L., Mandeville, C., Newman, S., 2002. SIMS analysis of volatiles in silicate glasses. Chem. Geol. 183, 99–114. https://doi.org/10.1016/S0009-2541(01)00375-8.

Hier-Majumder, S., Hirschmann, M.M., 2017. The origin of volatiles in the Earth's mantle. Geochem. Geophys. Geosyst. 18, 3078–3092. https://doi.org/10.1002/2017GC006937.

Hirose, K., Wood, B., Vočadlo, L., 2021. Light elements in the Earth's core. Nat. Rev. Earth. Environ. 2, 645–658. https://doi.org/10.1038/s43017-021-00203-6.

Hirschmann, M.M., 2018. Comparative deep Earth volatile cycles: the case for C recycling from exosphere/mantle fractionation of major (H_2O, C, N) volatiles and from H_2O/Ce, CO_2/Ba, and CO_2/Nb exosphere ratios. Earth. Planet. Sci. Lett. 502, 262–273. https://doi.org/10.1016/j.epsl.2018.08.023.

Hirschmann, M.M., Tenner, T., Aubaud, C., Withers, A.C., 2009. Dehydration melting of nominally anhydrous mantle: the primacy of partitioning. Phys. Earth Planet. Interior. 176, 54–68. https://doi.org/10.1016/j.pepi.2009.04.001.

Huang, R., Boffa Ballaran, T., McCammon, C.A., Frost, D.J., 2023. The composition and redox state of hydrous partial melts generated at the top of the lower mantle. Earth. Planet. Sci. Lett. 624 https://doi.org/10.1016/j.epsl.2023.118447.

Ito, E., Kubo, A., Katsura, T., Walter, M.J., 2004. Melting experiments of mantle materials under lower mantle conditions with implications for magma ocean differentiation. Phys. Earth Planet. Interior. 143, 397–406. https://doi.org/10.1016/j.pepi.2003.09.016.

Javoy, M., Kaminski, E., Guyot, F., Andrault, D., Sanloup, C., Moreira, M., Labrosse, S., Jambon, A., Agrinier, P., Davaille, A., Jaupart, C., 2010. The chemical composition of the Earth: enstatite chondrite models. Earth. Planet. Sci. Lett. 293, 259–268. https://doi.org/10.1016/j.epsl.2010.02.033.

Karki, B.B., Ghosh, D.B., Karato, S., 2021. Behavior and properties of water in silicate melts under deep mantle conditions. Sci. Rep. 11, 10588. https://doi.org/10.1038/s41598-021-90124-7.

Kawamoto, T., 2004. Hydrous phase stability and partial melt chemistry in H_2O-saturated KLB-1 peridotite up to the uppermost lower mantle conditions. Phys. Earth Planet. Interior. 143, 387–395. https://doi.org/10.1016/j.pepi.2003.06.003.

Kawamoto, T., Holloway, J.R., 1997. Melting temperature and partial melt chemistry of h2o-saturated mantle peridotite to 11 gigapascals. Science (1979) 276 (1979), 240–243. https://doi.org/10.1126/science.276.5310.240.
Kueter, N., Brugman, K., Miozzi, F., Cody, G.D., Yang, J., Strobel, T.A., Walter, M.J., 2023. Water speciation and hydrogen isotopes in hydrous stishovite: implications for the deep Earth water cycle. Contribut. Mineral. Petrol. 178, 48. https://doi.org/10.1007/s00410-023-02028-6.
Labrosse, S., Hernlund, J.W., Coltice, N., 2007. A crystallizing dense magma ocean at the base of the Earth's mantle. Nature 450, 866–869. https://doi.org/10.1038/nature06355.
Lebrun, T., Massol, H., Chassefière, E., Davaille, A., Marcq, E., Sarda, P., Leblanc, F., Brandeis, G., 2013. Thermal evolution of an early magma ocean in interaction with the atmosphere. J. Geophys. Res. Planets. 118, 1155–1176. https://doi.org/10.1002/jgre.20068.
Lesher, C.E., Walker, D., 1988. Cumulate maturation and melt migration in a temperature gradient. J. Geophys. Res. Solid. Earth. 93, 10295–10311. https://doi.org/10.1029/JB093iB09p10295.
Li, J., Lin, Y., Meier, T., Liu, Z., Yang, W., Mao, H., Zhu, S., Hu, Q., 2023. Silica-water superstructure and one-dimensional superionic conduit in Earth's mantle. Sci. Adv. 9 https://doi.org/10.1126/sciadv.adh3784.
Liebske, C., Corgne, A., Frost, D.J., Rubie, D.C., Wood, B.J., 2005. Compositional effects on element partitioning between Mg-silicate perovskite and silicate melts. Contribut. Mineral. Petrol. 149, 113–128. https://doi.org/10.1007/s00410-004-0641-8.
Liebske, C., Frost, D.J., 2012. Melting phase relations in the MgO-$MgSiO_3$ system between 16 and 26GPa: implications for melting in Earth's deep interior. Earth. Planet. Sci. Lett. 345–348, 159–170. https://doi.org/10.1016/j.epsl.2012.06.038.
Lin, Y., Hu, Q., Meng, Y., Walter, M., Mao, H.K., 2020. Evidence for the stability of ultrahydrous stishovite in Earth's lower mantle. Proc. Natl. Acad. Sci. U.S.A 117, 184–189. https://doi.org/10.1073/pnas.1914295117.
Lin, Y., Hu, Q., Walter, M.J., Yang, J., Meng, Y., Feng, X., Zhuang, Y., Cohen, R.E., Mao, H.-K., 2022. Hydrous SiO_2 in subducted oceanic crust and H_2O transport to the core-mantle boundary. Earth. Planet. Sci. Lett. 594, 117708 https://doi.org/10.1016/j.epsl.2022.117708.
Litasov, K., Ohtani, E., 2002. Phase relations and melt compositions in CMAS-pyrolite-H2O system up to 25GPa. Phys. Earth Planet. Interior. 134, 105–127. https://doi.org/10.1016/S0031-9201(02)00152-8.
Litasov, K.D., Kagi, H., Shatskiy, A., Ohtani, E., Lakshtanov, D.L., Bass, J.D., Ito, E., 2007. High hydrogen solubility in Al-rich stishovite and water transport in the lower mantle. Earth. Planet. Sci. Lett. 262, 620–634. https://doi.org/10.1016/j.epsl.2007.08.015.
Marty, B., 2012. The origins and concentrations of water, carbon, nitrogen and noble gases on Earth. Earth. Planet. Sci. Lett. 313–314, 56–66. https://doi.org/10.1016/j.epsl.2011.10.040.
Maurice, M., Tosi, N., Samuel, H., Plesa, A., Hüttig, C., Breuer, D., 2017. Onset of solid-state mantle convection and mixing during magma ocean solidification. J. Geophys. Res. Planets. 122, 577–598. https://doi.org/10.1002/2016JE005250.
McDonough, W.F., Sun, S.s., 1995. The composition of the Earth. Chem Geol 120, 223–253. https://doi.org/10.1016/0009-2541(94)00140-4.
Mibe, K., Kanzaki, M., Kawamoto, T., Matsukage, K.N., Fei, Y., Ono, S., 2007. Second critical endpoint in the peridotite-H2O system. J. Geophys. Res. Solid. Earth. 112 https://doi.org/10.1029/2005JB004125.
Miyazaki, Y., Korenaga, J., 2022. A wet heterogeneous mantle creates a habitable world in the Hadean. Nature 603, 86–90. https://doi.org/10.1038/s41586-021-04371-9.
Miyazaki, Y., Korenaga, J., 2019. On the timescale of magma ocean solidification and its chemical consequences: 2. Compositional differentiation under crystal accumulation and matrix compaction. J. Geophys. Res. Solid. Earth. 124, 3399–3419. https://doi.org/10.1029/2018JB016928.
Monteux, J., Andrault, D., Guitreau, M., Samuel, H., Demouchy, S., 2020. A mushy Earth's mantle for more than 500Myr after the magma ocean solidification. Geophys. J. Int. 221, 1165–1181. https://doi.org/10.1093/gji/ggaa064.
Monteux, J., Andrault, D., Samuel, H., 2016. On the cooling of a deep terrestrial magma ocean. Earth. Planet. Sci. Lett. 448, 140–149. https://doi.org/10.1016/j.epsl.2016.05.010.
Murakami, M., Ohishi, Y., Hirao, N., Hirose, K., 2012. A perovskitic lower mantle inferred from high-pressure, high-temperature sound velocity data. Nature 485, 90–94. https://doi.org/10.1038/nature11004.
Myhill, R., Frost, D.J., Novella, D., 2017. Hydrous melting and partitioning in and above the mantle transition zone: insights from water-rich MgO–SiO_2–H_2O experiments. Geochim. Cosmochim. Acta 200, 408–421. https://doi.org/10.1016/j.gca.2016.05.027.
Nakajima, A., Sakamaki, T., Kawazoe, T., Suzuki, A., 2019. Hydrous magnesium-rich magma genesis at the top of the lower mantle. Sci. Rep. 9 https://doi.org/10.1038/s41598-019-43949-2.
Newcombe, M.E., Nielsen, S.G., Peterson, L.D., Wang, J., Alexander, C.M.O., Sarafian, A. R., Shimizu, K., Nittler, L.R., Irving, A.J., 2023. Degassing of early-formed planetesimals restricted water delivery to Earth. NatureNature 615, 854–857. https://doi.org/10.1038/s41586-023-05721-5.
Nisr, C., Chen, H., Leinenweber, K., Chizmeshya, A., Prakapenka, V.B., Prescher, C., Tkachev, S.N., Meng, Y., Liu, Z., Shim, S.-H., 2020. Large H_2O solubility in dense silica and its implications for the interiors of water-rich planets. Proc. Natl. Acad. Sci. 117, 9747–9754. https://doi.org/10.1073/pnas.1917448117.
Nisr, C., Leinenweber, K., Prakapenka, V., Prescher, C., Tkachev, S., Shim, S.-H.D., 2017. Phase transition and equation of state of dense hydrous silica up to 63GPa. J. Geophys. Res. Solid. Earth. 122, 6972–6983. https://doi.org/10.1002/2017JB014055.
Nomura, R., Ozawa, H., Tateno, S., Hirose, K., Hernlund, J., Muto, S., Ishii, H., Hiraoka, N., 2011. Spin crossover and iron-rich silicate melt in the Earth's deep mantle. NatureNature 473, 199–202. https://doi.org/10.1038/nature09940.
Ohtani, E., 2021. Hydration and dehydration in earth's interior. Annu Rev. Earth. Planet. Sci. 49, 253–278. https://doi.org/10.1146/annurev-earth-080320-062509.
Peslier, A.H., Schönbächler, M., Busemann, H., Karato, S.-I., 2017. Water in the Earth's interior: distribution and Origin 83–150. https://doi.org/10.1007/978-94-024-1628-2_4.
Peterson, L.D., Newcombe, M.E., Alexander, C.M.O., Wang, J., Sarafian, A.R., Bischoff, A., Nielsen, S.G., 2023. The H_2O content of the ureilite parent body. Geochim. Cosmochim. Acta 340, 141–157. https://doi.org/10.1016/j.gca.2022.10.036.
Pierru, R., Andrault, D., Manthilake, G., Monteux, J., Devidal, J.L., Guignot, N., King, A., Henry, L., 2022. Deep mantle origin of large igneous provinces and komatiites. Sci. Adv. 8 https://doi.org/10.1126/sciadv.abo1036.
Schmandt, B., Jacobsen, S.D., Becker, T.W., Liu, Z., Dueker, K.G., 2014. Dehydration melting at the top of the lower mantle. Science (1979) 344 (1979), 1265–1268. https://doi.org/10.1126/science.1253358.
Shatskiy, A., Fukui, H., Matsuzaki, T., Shinoda, K., Yoneda, A., Yamazaki, D., Ito, E., Katsura, T., 2007. Growth of large (1 mm) $MgSiO_3$ perovskite single crystals: a thermal gradient method at ultrahigh pressure. Am. Mineral. 92, 1744–1749. https://doi.org/10.2138/am.2007.2415.
Shimizu, K., Alexander, C.M.O., Hauri, E.H., Sarafian, A.R., Nittler, L.R., Wang, J., Jacobsen, S.D., Mendybaev, R.A., 2021. Highly volatile element (H, C, F, Cl, S) abundances and H isotopic compositions in chondrules from carbonaceous and ordinary chondrites. Geochim. Cosmochim. Acta 301, 230–258. https://doi.org/10.1016/j.gca.2021.03.005.
Shirey, S.B., Wagner, L.S., Walter, M.J., Pearson, D.G., van Keken, P.E., 2021. Slab transport of fluids to deep focus earthquake depths—Thermal modeling constraints and evidence from diamonds. AGU Adv. 2 https://doi.org/10.1029/2020AV000304.
Solomatov, V., 2007. Magma oceans and primordial mantle differentiation. Treatise Geophys. 9, 91–119. https://doi.org/10.1016/b978-044452748-6/00141-3.
Stixrude, L., de Koker, N., Sun, N., Mookherjee, M., Karki, B.B., 2009. Thermodynamics of silicate liquids in the deep Earth. Earth. Planet. Sci. Lett. 278, 226–232. https://doi.org/10.1016/j.epsl.2008.12.006.
Stixrude, L., Lithgow-Bertelloni, C., 2011. Thermodynamics of mantle minerals - II. Phase equilibria. Geophys. J. Int. 184, 1180–1213. https://doi.org/10.1111/j.1365-246X.2010.04890.x.
Tonks, W.B., Melosh, H.J., 1993. Magma ocean formation due to giant impacts. J. Geophys. Res. 98, 5319–5333. https://doi.org/10.1029/92JE02726.
Tonks, W.B., Melosh, H.J., 1990. The physics of crystal settling and suspension in a turbulent magma ocean. Origin of the Earth, pp. 151–174.
Walter, M.J., Nakamura, E., Trønnes, R.G., Frost, D.J., 2004. Experimental constraints on crystallization differentiation in a deep magma ocean. Geochim. Cosmochim. Acta 68, 4267–4284. https://doi.org/10.1016/j.gca.2004.03.014.
Walter, M.J., Thomson, A.R., Wang, W., Lord, O.T., Ross, J., McMahon, S.C., Baron, M.A., Melekhova, E., Kleppe, A.K., Kohn, S.C., 2015. The stability of hydrous silicates in Earth's lower mantle: experimental constraints from the systems MgO-SiO_2-H_2O and MgO-Al_2O_3-SiO_2-H_2O. Chem Geol 418, 16–29. https://doi.org/10.1016/j.chemgeo.2015.05.001.
Wang, H.S., Lineweaver, C.H., Ireland, T.R., 2018. The elemental abundances (with uncertainties) of the most Earth-like planet. Icarus 299, 460–474. https://doi.org/10.1016/j.icarus.2017.08.024.
Wang, J., Takahashi, E., Xiong, X., Chen, L., Li, L., Suzuki, T., Walter, M.J., 2020. The water-saturated solidus and second critical endpoint of peridotite: implications for magma genesis within the mantle wedge. J. Geophys. Res. Solid. Earth. 125 https://doi.org/10.1029/2020JB019452.
Wasson, J.T., Kallemeyn, G.W., 1988. Compositions of chondrites. Philos. Trans. R. Soc. Lond. Ser. A, Math. Phys. Sci. 325, 535–544. https://doi.org/10.1098/rsta.1988.0066.
Xie, L., Yoneda, A., Katsura, T., Andrault, D., Tange, Y., Higo, Y., 2021. Direct viscosity measurement of peridotite melt to lower-mantle conditions: a further support for a fractional magma-ocean solidification at the top of the lower mantle. Geophys. Res. Lett. https://doi.org/10.1029/2021GL094507.
Xie, L., Yoneda, A., Yamazaki, D., Manthilake, G., Higo, Y., Tange, Y., Guignot, N., King, A., Scheel, M., Andrault, D., 2020. Formation of bridgmanite-enriched layer at the top lower-mantle during magma ocean solidification. Nat. Commun. 11 https://doi.org/10.1038/s41467-019-14071-8.
Yang, Y.-N., Du, Z., Lu, W., Qi, Y., Zhang, Y.-Q., Zhang, W.-F., Zhang, P.-F., 2023. NanoSIMS analysis of water content in bridgmanite at the micron scale: an experimental approach to probe water in Earth's deep mantle. Front. Chem. 11 https://doi.org/10.3389/fchem.2023.1166593.
Yao, J., Frost, D.J., Steinle-Neumann, G., 2021. Lower mantle melting: experiments and thermodynamic modeling in the system MgO-SiO_2. J. Geophys. Res. Solid. Earth. 126 https://doi.org/10.1029/2021JB022568.
Yoshino, T., Nishihara, Y., Karato, S., 2007. Complete wetting of olivine grain boundaries by a hydrous melt near the mantle transition zone. Earth. Planet. Sci. Lett. 256, 466–472. https://doi.org/10.1016/j.epsl.2007.02.002.
Zhang, J., Herzberg, C., 1994. Melting experiments on anhydrous peridotite KLB-1. J. Geophys. Res. 99742, 729. –17.